

# Numerical Simulation of Electroosmotic Flow

Neelesh A. Patankar<sup>†</sup> and Howard H. Hu\*

Department of Mechanical Engineering and Applied Mechanics, University of Pennsylvania, Philadelphia, Pennsylvania 19104-6315

**We have developed a numerical scheme to simulate electroosmotic flows in complicated geometries. We studied the electroosmotic injection characteristics of a cross-channel device for capillary electrophoresis. We found that the desired rectangular shape of the sample plug at the intersection of the cross-channel can be obtained when the injection is carried out at high electric field intensities. The shape of the sample plug can also be controlled by applying an electric potential or a pressure at the side reservoirs. Flow induced from the side channels into the injection channel squeezes the streamlines at the intersection, thus giving a less distorted sample plug. Results of our simulations agree qualitatively with experimental observations.**

Extensive experimental studies of capillary electrophoresis using micromachined channels have been performed recently. Harrison et al.<sup>1</sup> integrated a capillary electrophoresis and sample injection system on a planar glass chip. They observed that the solvent flow could be directed along a specified capillary by the application of appropriate voltages, so that valveless switching of fluid flow between the capillaries could be achieved. Seiler et al.<sup>2</sup> presented improvements in the instrumentation and experimental method for the device described by Harrison et al.<sup>1</sup> Harrison et al.<sup>3</sup> performed electroosmotic pumping and electrophoretic separation of samples using a device consisting of two intersecting channels micromachined in silicon. Fan and Harrison<sup>4</sup> used a similar cross-channel device integrated on a glass chip and evaluated its performance. Seiler et al.<sup>5</sup> used a device in which the electroosmotic flow was driven within a network of intersecting capillaries integrated on a glass chip. Kirchoff's rules for resistive networks were found to predict the fluid flow within the capillaries. Effenhauser et al.<sup>6</sup> performed high-speed separation of antisense oligonucleotides on a micromachined capillary electrophoresis device integrated on a glass plate. Burggraf et al.<sup>7</sup> presented a

novel approach for the ion separation in solutions using the concept of synchronized cyclic capillary electrophoresis. Repeated column switching during the capillary electrophoresis eliminated the unwanted sample components and separated the species having very similar mobilities. Jacobson et al.<sup>8</sup> did capillary electrophoresis in a cross-channel device with an integrated postcolumn reactor. The device was fabricated on a glass plate. A postcolumn reactor was added to conduct postseparation derivatization using a fluorescent "tag" for amino acids. Culbertson and Jorgenson<sup>9</sup> suggested a new approach for increasing the efficiency and resolution of the capillary electrophoresis. The approach utilized a pressure-induced counterflow to actively retard, halt, or reverse the electrokinetic migration of an analyte, thus keeping the analytes of interest in the separation field much longer than under the normal separation conditions.

In most of these experiments, the injection of the sample into the separation channel was achieved using the electroosmotic flow driven by an applied potential along the injection channel. The injection channel and the separation channel were perpendicular to each other, although the overall design of the device might not be as simple as a cross-channel. The shape of the inserted sample, which is an important parameter that influences the resolution of the separated zones during the electrophoresis, depends primarily on the electroosmotic flow pattern at the intersection of the channels. The electroosmotic flow at the intersection itself is influenced by various parameters. Until now only experimental investigations have been performed to determine the parameters that give the most desirable shape of the injected sample. However, it would be more suitable to do such investigations through numerical simulations since one can better control various parameters involved.

Rice and Whitehead<sup>10</sup> formulated the equations for the electroosmotic flow in a capillary. Jorgenson and Lukacs<sup>11</sup> developed a one-dimensional model for the capillary electrophoresis. Andreev and Lisin<sup>12</sup> presented a mathematical model for one-dimensional capillary electrophoresis and studied the influence of the electroosmotic flow profile on the efficiency of separation. A three-dimensional model is required to study the electroosmotic flow in more complicated geometries.

In this work, we tested a three-dimensional model for electroosmotic flows. The primary aim is to develop a robust

<sup>†</sup> Present address: Department of Aerospace Engineering and Mechanics, University of Minnesota, Minneapolis, MN 55455.

- (1) Harrison, D. J.; Manz, A.; Fan, Z.; Lüdi, H.; Widmer, H. M. *Anal. Chem.* **1992**, *64*, 1926–1932.
- (2) Seiler, K.; Harrison, D. J.; Manz, A. *Anal. Chem.* **1993**, *65*, 1481–1488.
- (3) Harrison, D. J.; Glavina, P. G.; Manz, A. *Sens. Actuators, B* **1993**, *10*, 107–116.
- (4) Fan, Z. H.; Harrison, D. J. *Anal. Chem.* **1994**, *66*, 177–184.
- (5) Seiler, K.; Fan, Z. H.; Fluri, K.; Harrison, D. J. *Anal. Chem.* **1994**, *66*, 3485–3491.
- (6) Effenhauser, C. S.; Paulus, A.; Manz, A.; Widmer, H. M. *Anal. Chem.* **1994**, *66*, 2949–2953.
- (7) Burggraf, N.; Manz, A.; Verpoorte, E.; Effenhauser, C. S.; Widmer, H. M. *Sens. Actuators, B* **1994**, *20*, 103–110.

- (8) Jacobson, S. C.; Koutny, L. B.; Hergenroder, R.; Moore, A. W., Jr.; Ramsey, J. M. *Anal. Chem.* **1994**, *66*, 3472–3476.
- (9) Culbertson, C. T.; Jorgenson, J. W. *Anal. Chem.* **1994**, *66*, 955–962.
- (10) Rice, C. I.; Whitehead, R. *J. Phys. Chem.* **1965**, *69*, 4017–4024.
- (11) Jorgenson, J. M.; Lukacs, K. D. *Anal. Chem.* **1981**, *53*, 1298–1302.
- (12) Andreev, V. P.; Lisin, E. E. *Chromatogr.* **1993**, *37*, 202–210.

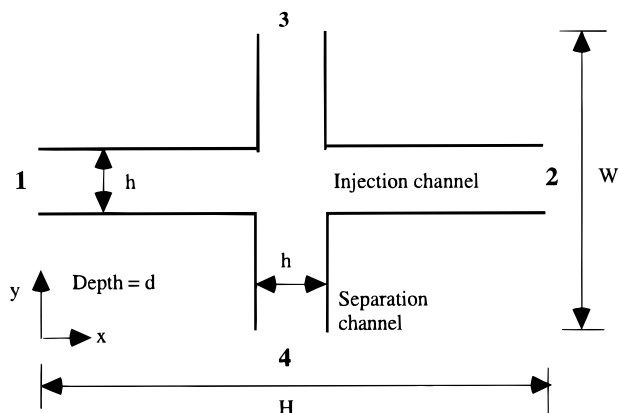


Figure 1. Cross-channel device.

numerical scheme that can be applied to various flow conditions. As an example we simulate the electroosmotic flow at the intersection of a cross-channel during the injection process. These simulations help to determine the parameters that are important in controlling the shape of the injected sample. Fan and Harrison<sup>4</sup> studied such a device experimentally. Our findings will be qualitatively compared with their conclusions. Such a comparison will validate the predictions made by our simulations, thus establishing a reliable scheme to simulate electroosmotic flows in more complicated geometries.

#### DESCRIPTION OF THE GEOMETRY

The geometry of the device used by Fan and Harrison<sup>4</sup> is similar to that shown in Figure 1. There is an intersection of cross-channels with four reservoirs numbered 1–4. The cross-channels are closed by walls from above and below. The injection of the sample solution (containing various species) is effected by applying an electric potential between reservoirs 1 and 2. This potential drives the sample solution from reservoir 1 across the intersection, creating a sample plug in the path between reservoirs 3 and 4. Sample separation does not occur during the injection, since the sample solution runs continuously in the injection channel. The separation of the species in the sample requires the sample to be arranged initially in a zone so that the species can move away from each other due to the difference in their electrophoretic mobilities (as the zone spreads).<sup>13</sup> During the separation process, the electric potential between reservoirs 3 and 4 drives the sample plug to move toward reservoir 4 and causes the separation of various species.

In our numerical simulation, we intend to study the flow pattern in the injection phase, i.e., when the sample is injected by applying a potential between reservoirs 1 and 2. Clearly the shape of the sample at the intersection depends largely on the flow pattern at the intersection and on the diffusion of the sample into the buffer solution. For reasons to be described later, we will be neglecting the diffusion of the sample. Besides, we will only study the steady-state flow pattern at the intersection.

#### PROBLEM FORMULATION

Unless the sample is allowed to stay at the intersection for a long time, the diffusion of the sample solution from the injection

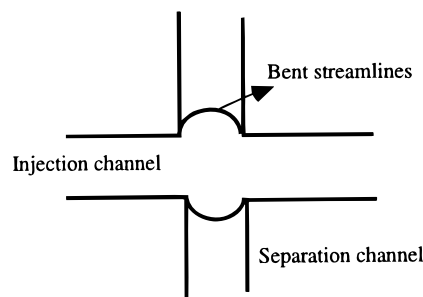


Figure 2. Bent streamlines at the intersection.

channel into the separation channel is not important, since the diffusion time is much longer than the relevant convective time scale of the flow. This will become clear from the subsequent discussion. The equation for the diffusion of the sample is

$$\frac{\partial C}{\partial t} + (\mathbf{V} \cdot \nabla) C = D \nabla^2 C \quad (1)$$

where  $C$  is the sample concentration,  $\mathbf{V}$  is the flow velocity, and  $D$  is the diffusion coefficient. Let  $U$  be the convective velocity scale and  $h$  be some length scale, e.g. the channel width. If we nondimensionalize the velocity by  $U$ , length by  $h$ , and time by  $h/U$ , (1) becomes (we retain the same symbols for the nondimensional variables)

$$\frac{\partial C}{\partial t} + (\mathbf{V} \cdot \nabla) C = \frac{1}{ScRe} D \nabla^2 C \quad (2)$$

where the nondimensional parameters  $Sc = \nu/D$  is the Schmidt number and  $Re = Uh/\nu$  is the Reynolds number.  $\nu$  is the kinematic viscosity of the sample solution. For the problem at hand,  $D$  is of the order of  $10^{-11}$  m<sup>2</sup>/s, and  $\nu$  is of the order of  $10^{-6}$  m<sup>2</sup>/s; thus  $Sc$  is of the order of  $10^5$  and  $Re$  is of order one. Therefore, the diffusion is negligible as compared to the convection, since  $Sc \cdot Re$  is large. This means that the sample species convect with the flow. Consequently, the solution of the flow field should give a fairly good idea regarding the concentration distribution of the sample.

An efficient and accurate separation requires a rectangular sample plug at the intersection of the channels. Straight streamlines (or particle path lines) at the intersection are desirable. However, the streamlines at the intersection will generally be "bent" (Figure 2). After the injection starts, the initially straight streamlines will bend more and more at the intersection as the flow progresses toward the steady state. The flow pattern at the steady state will exaggerate the distortion of the sample shape at the intersection and will give a "conservative" prediction regarding the parameters most suitable for the desired rectangular sample shape. Unsteady simulations are computationally costly since the flow field is to be solved at each time step instead of just once as in the steady case. Given the above argument, we choose to perform only steady simulations. It should be noted that unsteady simulations can provide information regarding the duration of injection (discussed later). This information is not accessible through the steady simulation.

During the injection, some part of the cross-channel will be occupied by the buffer solution while the rest will be occupied by

(13) Saville, D. A.; Palusinski, O. A. *AIChE J.* **1986**, *32*, 207–214.

the sample solution. Since the sample solution is generally a dilute solution of certain species in the buffer, we assume that the mechanical properties of the sample solution are the same as that of the buffer. Therefore, only one type of the solution is to be considered in the entire cross-channel. The Joule heating, which gives rise to temperature variations in the channels, may also make the properties of the solution nonuniform. However, since we are considering the capillary electrophoresis where temperature variations are usually small due to the efficient heat dissipation, we can neglect the Joule heating and assume that the mechanical properties of the solution in the cross-channel are uniform.

Given the above assumptions, the basic equations describing the flow are the continuity equation,

$$\nabla \cdot \mathbf{V} = 0 \quad (3)$$

and the momentum equation,

$$\rho \left[ \frac{\partial \mathbf{V}}{\partial t} + (\mathbf{V} \cdot \nabla) \mathbf{V} \right] = -\nabla p + \mu \nabla^2 \mathbf{V} + \rho_e \mathbf{E} \quad (4)$$

where  $\mathbf{V}$  is the velocity,  $\rho$  is the density,  $p$  is the pressure,  $\mu$  is the viscosity,  $\rho_e$  is the electric charge density, and  $\mathbf{E}$  is the electric field intensity. The electric field is related to the electric potential  $\Phi$  by,

$$\mathbf{E} = -\nabla \Phi \quad (5)$$

while the electric potential is governed by,

$$\nabla^2 \Phi = -(\rho_e/\epsilon) \quad (6)$$

where  $\epsilon$  is the electrical permittivity of the solution. Substituting eqs 5 and 6 into eq 4, the momentum equation can be rewritten as,

$$\rho \left[ \frac{\partial \mathbf{V}}{\partial t} + (\mathbf{V} \cdot \nabla) \mathbf{V} \right] = -\nabla p + \mu \nabla^2 \mathbf{V} + \epsilon [\nabla^2 \Phi \cdot \nabla \Phi] \quad (7)$$

Equations 5 and 6 can be modified to obtain a more solvable form. The channel walls in contact with the solution have a certain potential due to the charge on them. This potential is called the  $\zeta$  potential. The electroosmotic flow is primarily caused by the migration of the charged species next to the channel walls subjected to an externally applied electric field. The distribution of the charged species in the domain is governed by the potential at the walls and by the externally applied electric field. When the Debye thickness is small and the charge at the walls is not large, this distribution is governed mainly by the  $\zeta$  potential at the wall and is affected very little by the external electric field.<sup>14</sup> Thus, the charge distribution near the walls can be determined independent of the external electric field. The charge distribution may be affected by fluid motion since the charged species convect with the flow. However, the effect of fluid motion on the charge redistribution can be neglected when the fluid velocity is small,

i.e., when the inertial terms in the momentum equation are not dominant<sup>14</sup> or when the Debye thickness is small. This will be explained later. In summary, the electric field equations and the fluid flow equations can be decoupled, and the potential  $\Phi$  can be decomposed into a potential due to the external electric field,  $\phi$ , and a potential due to the charge at the walls,  $\psi$ ,<sup>15</sup>

$$\Phi = \phi + \psi \quad (8)$$

Consequently (6) can be written as two separate equations,

$$\nabla^2 \phi = 0 \quad (9)$$

and

$$\nabla^2 \psi = -(\rho_e/\epsilon) \quad (10)$$

The external electric field, which generates a force on the charged species causing the electroosmotic flow, is given by

$$\mathbf{E} = -\nabla \phi \quad (11)$$

This decomposition is similar to that given by Grossman and Colburn.<sup>16</sup> Equation 10 can be further simplified following a treatment similar to that of Hiemenz<sup>17</sup> where two important steps are involved. First is the use of an expression for the number density of ions in solution near a charged surface as proposed by Debye and Hückel, and in the second step, the Debye–Hückel approximation was made to further simplify this expression. Details of the steps applied to the one-dimensional case can be found in ref 16. They obtained the following simplified one-dimensional form of (10),

$$\frac{d^2 \psi}{dx^2} = \kappa^2 \psi \quad (12)$$

where  $\kappa^{-1}$  is called the Debye length and it corresponds to the thickness of the Debye layer. The Debye length is generally a constant for a given solid–liquid interface. For the cross-channel geometry, we need a simplified three-dimensional form of (12). Similar to Henry<sup>15</sup> we generalize (12) to the three-dimensional form

$$\nabla^2 \psi = \kappa^2 \psi \quad (13)$$

From (10) and (13) we get the following expression for the charge density,

$$\rho_e = -\epsilon \kappa^2 \psi \quad (14)$$

Using (11) and (14), we rewrite the momentum eq 4 as,

(15) Henry, D. C. *Proc. R. Soc. London Ser. A.* **1931**, *133*, 106–129.

(16) Grossman, P. D.; Colburn, J. C. *Capillary Electrophoresis, Theory & Practice*; Academic Press: San Diego, 1992.

(17) Hiemenz, P. C. *Principles of Colloid and Surface Chemistry*, 2nd ed.; Marcel Dekker: New York, 1986.

(14) Saville, D. A. *Annu. Rev. Fluid Mech.* **1977**, *9*, 321–337.

$$\rho \left[ \frac{\partial \mathbf{V}}{\partial t} + (\mathbf{V} \cdot \nabla) \mathbf{V} \right] = -\nabla p + \mu \nabla^2 \mathbf{V} + \epsilon \kappa^2 \psi \nabla \phi \quad (15)$$

Similar equations were obtained by Saville<sup>14</sup> by using perturbation methods for the flow around a charged particle.

We nondimensionalize the variables by scaling the length by the channel width  $h$  (Figure 1), the potential  $\phi$  by the value of the potential ( $\varphi$ ) applied at reservoir 1 during the injection of the sample while reservoir 2 is grounded, the potential  $\psi$  by the zeta potential  $\zeta$ , the velocity  $\mathbf{V}$  by  $\varphi \epsilon \zeta / \mu H$ , where  $H$  is the distance between reservoirs 1 and 2 (Figure 1) and the pressure by  $\varphi \epsilon \zeta / hH$ . Retaining the variable names as before, the relevant nondimensionalized equations can be rewritten as,

$$\left. \begin{aligned} \nabla \cdot \mathbf{V} &= 0 \\ Re \left[ \frac{\partial \mathbf{V}}{\partial t} + (\mathbf{V} \cdot \nabla) \mathbf{V} \right] &= -\nabla p + \nabla^2 \mathbf{V} + (\kappa^2 h H) \psi \nabla \phi \\ \nabla^2 \psi &= (\kappa h)^2 \psi \\ \nabla^2 \phi &= 0 \end{aligned} \right\} \quad (16)$$

where  $Re$  is the flow Reynolds number defined as,

$$Re = \rho \left( \frac{\varphi \epsilon \zeta}{\mu H} \right) \left( \frac{h}{\mu} \right) \quad (17)$$

Note that the equations for the two potentials are decoupled from the fluid equations and can be solved independent of the flow field, while the fluid flow depends on the potential field through the body force term.

The main parameters of the problem are the Reynolds number  $Re$ , the nondimensional Debye thickness  $(\kappa h)^{-1}$ , the potentials applied at reservoirs 3 and 4, and  $H/h$ . In the simulations, we fixed the channel geometry,  $H/h = 50$ ,  $W/h = 30$ , and  $d/h = 1/3$ , where  $d$  is the channel depth. In the device used by Fan and Harrison,<sup>4</sup> the channel width  $h = 30 \mu\text{m}$ . We will be studying the effects of the Reynolds number and the potentials at the side reservoirs.

We need to specify the boundary conditions for the problem. For the potential due to the external electric field,  $\phi$ , we impose the insulation condition at the side, top, and bottom walls,<sup>14,15</sup> and nondimensionalized values of 1 at reservoir 1 and 0 at reservoir 2. At reservoirs 3 and 4, we impose a constant potential which is one of the parameters we adjust in the simulations. Different values for this potential will produce different flow patterns at the intersection of the channels.

For the potential due to the surface charge,  $\psi$ , we impose a constant nondimensionalized value of  $-1$  (the  $\zeta$  potential) on all walls. This implies that the wall is negatively charged and will form a thin layer of positively charged species next to itself. Application of a positive electric field will induce a fluid velocity in the positive  $x$  direction. We impose "insulation-type" boundary condition at the reservoirs for potential  $\psi$ .

For the flow field, we should ideally impose a velocity boundary condition at all reservoirs and on the walls and need to specify a location for a reference pressure. However, it is not straightforward to impose a velocity condition at the reservoirs since it is not known a priori. The driving force in the system of eqs 16 is the body force acting on the fluid due to the externally applied

electric field. This body force generates a velocity at the reservoirs that is part of the solution. Hence, it is preferable to come up with a more convenient set of boundary conditions which still captures the physical nature of the problem. After a few trials, we have concluded that such suitable set of boundary condition is a "fully developed" velocity profile at the reservoirs:

$$\mathbf{V} = [v_x(y,z) \quad 0 \quad 0], \quad \frac{\partial \mathbf{V}}{\partial x} = 0, \quad \text{at reservoirs 1 and 2} \quad (18)$$

and

$$\mathbf{V} = [0 \quad v_y(x,z) \quad 0], \quad \frac{\partial \mathbf{V}}{\partial y} = 0, \quad \text{at reservoirs 3 and 4} \quad (19)$$

where the coordinates  $x$  and  $y$  are indicated in the Figure 1. While using these boundary conditions, it is also necessary to impose an additional condition for the overall mass conservation; i.e., there should be no net flux into the computation domain.

As in the experiments, we set the pressure to zero over the entire cross section of the channel at each reservoir,

$$p = 0 \quad \text{at all the reservoirs} \quad (20)$$

Equations 18–20 represent a set of overspecified boundary conditions, but they are consistent. When the velocity profile in a channel is fully developed, it can be shown that the pressure is uniform over the entire cross section.

When the flow is being driven by the electric field as well as by an externally applied pressure gradient, we need to specify the values of pressure at the corresponding reservoirs in (20). Other boundary conditions remain the same. The applied pressure gradient will drive the flow in addition to the electroosmotic flow. Some researchers used this technique to control the sample injection process.

#### DISCUSSION ON THE DURATION OF INJECTION

Fan and Harrison<sup>4</sup> reported that the duration of the sample injection affects the separation efficiency. The separation efficiency depends on the shape of the injected sample, which in turn relies on the electroosmotic flow pattern at the intersection of the channels. They observed that the separation efficiency increased as the duration of the injection was increased until some time  $t_c$  after which it dropped significantly. Such a behavior might be related to the unsteady flow field and/or the time it takes for the sample to fill the intersection of the cross-channel. It is thus necessary to carry out relevant simulations to answer these questions. The time  $t_c$ , observed by Fan and Harrison,<sup>4</sup> may correspond to the time for the flow to reach the steady state. To see this we will estimate the time for the electroosmotic flow to reach the steady state in a two-dimensional straight channel.

The nondimensional eqs 16 for an electroosmotic flow in a two-dimensional straight channel can be reduced to

$$d^2 \psi / dy^2 = (\kappa h)^2 \psi \quad (21)$$

$$Re \frac{\partial v_x}{\partial t} = \frac{\partial^2 v_x}{\partial y^2} - (\kappa h)^2 \psi \quad (22)$$

where we have nondimensionalized the length by the channel width  $h$ , the potential  $\psi$  by the  $\zeta$  potential at the walls, the velocity along the channel,  $v_x$ , by  $E\zeta/\mu$ .  $E$  is the externally applied electric field, and  $y$  is the direction perpendicular to the channel length. The boundary conditions are  $\psi = 1$  and  $v_x = 0$  at the channels walls  $y = 0$  and  $y = 1$ . We have taken the  $\zeta$  potential to be positive; hence there will be a layer of negative charges next to the wall. A positive value of externally applied electric field will thus cause a flow in the negative  $x$  direction. The solution for  $\psi$  is given by

$$\psi = \frac{\cosh[\kappa h(y - 1/2)]}{\cosh[\kappa h/2]} \quad (23)$$

and the solution for the velocity takes the form,

$$v_x(y, t) = \left( \frac{\cosh[\kappa h(y - 1/2)]}{\cosh[\kappa h/2]} - 1 \right) - \sum_{n=1}^{\infty} e^{-(n^2\pi^2 t/Re)} A_n \sin(n\pi y) \quad (24)$$

where the first term represents the steady-state solution and the coefficients  $A_n$  should be determined from the initial condition  $v_x(y, 0) = 0$ .

From (24) we observe that  $n = 1$  is the strongest mode and decays the slowest in time. Hence the rate of the solution approaches the steady state can be represented by the rate at which the exponential  $e^{-(\pi^2/Re)t}$  approaches zero. We may decide that the time at which this exponential reduces to 0.01 is the time,  $t_{ss}$ , required to reach the steady state,

$$t_{ss} = 0.467Re \quad (25)$$

This time is nondimensional. The actual dimensional time,  $T_{ss}$ , required to reach the steady state is given by

$$T_{ss} = 0.467h^2/\nu \quad (26)$$

where  $\nu$  is the kinematic viscosity. We observe that the time to reach the steady state depends only on the channel width and the fluid viscosity.

In the experiments by Fan and Harrison,<sup>4</sup> the channel width was  $30 \mu\text{m}$ . The estimate for the time for the electroosmotic flow to reach the steady state in this two-dimensional channel is around  $T_{ss} = 0.42$  ms. However, the flow at the intersection might take much longer time to reach the steady state. In the experiments by Fan and Harrison,<sup>4</sup> they observed that  $t_e \sim 50-100$  ms. Their observation must be related to the unsteady flow field at the intersection.

#### DISCUSSION ON THE SINGULARITY AT THE CORNERS

The nature of the equations for the electric potentials suggests that there might exist singular behavior at the corners of the channels. In this section, we intend to study the nature of this singularity for both  $\phi$  and  $\psi$  fields. We will consider a two-dimensional analysis of the potential field inside a wedge as shown in Figure 3.

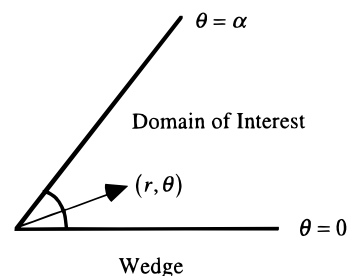


Figure 3. Domain for singularity analysis.

For the external electric potential  $\phi$ , the governing equation in the polar coordinate system becomes

$$\frac{1}{r} \frac{\partial}{\partial r} \left( r \frac{\partial \phi}{\partial r} \right) + \frac{1}{r^2} \frac{\partial^2 \phi}{\partial \theta^2} = 0 \quad (27)$$

with

$$\frac{\partial \phi}{\partial \theta} = 0 \quad \text{at} \quad \theta = 0 \quad \text{and} \quad \theta = \alpha$$

Solving (27) by separation of variables we get

$$\phi(r, \theta) = \sum_{n=1}^{\infty} A_n r^{n\pi/\alpha} \cos\left(\frac{n\pi\theta}{\alpha}\right) \quad (28)$$

where  $A_n$  depends on the far field boundary condition. At the corner ( $r \rightarrow 0$ ) the leading order terms for  $\phi$  and  $\nabla\phi$  are

$$\begin{aligned} \phi &\sim A_1 r^{\pi/\alpha} \cos(\pi\theta/\alpha) \\ \nabla\phi &\sim A_1 \frac{\pi}{\alpha} r^{(\pi/\alpha)-1} \left[ \cos\left(\frac{\pi\theta}{\alpha}\right) \hat{\mathbf{r}} - \sin\left(\frac{\pi\theta}{\alpha}\right) \theta \right] \end{aligned} \quad (29)$$

where  $\hat{\mathbf{r}}$  and  $\theta$  are unit vectors in the radial and angular directions, respectively. From (29) we note that  $\nabla\phi \rightarrow \infty$  as  $r \rightarrow 0$  for  $\alpha > \pi$ , whereas  $\phi$  is always bounded. Thus, there is an integrable singularity at the corner for the potential  $\phi$  when  $\alpha > \pi$ .

For the surface charge potential  $\psi$ , let  $\psi_w$  be the  $\zeta$  potential at the walls, we have the governing equations,

$$\begin{aligned} \frac{1}{r} \frac{\partial}{\partial r} \left( r \frac{\partial \psi}{\partial r} \right) + \frac{1}{r^2} \frac{\partial^2 \psi}{\partial \theta^2} - \kappa^2 \psi &= 0 \\ \text{with } \psi &= \psi_w \text{ at } \theta = 0 \text{ and } \theta = \alpha \end{aligned} \quad (30)$$

The local solution for (30) around the corner  $r = 0$  takes the form of,

$$\psi(r, \theta) = \psi_w + \sum_{n=1}^{\infty} D_n r^{n\pi/\alpha} \sin\left(\frac{n\pi\theta}{\alpha}\right) \quad (31)$$

where  $D_n$  depends on the far field boundary condition. At the corner  $r = 0$ , the leading order terms for  $\psi$  and  $\nabla\psi$  are

$$\psi \sim \psi_w + D_1 r^{\pi/\alpha} \sin\left(\frac{\pi\theta}{\alpha}\right)$$

$$\nabla\psi \sim D_1 \frac{\pi}{\alpha} r^{(\pi/\alpha)-1} \left[ \sin\left(\frac{\pi\theta}{\alpha}\right) \hat{\mathbf{r}} + \cos\left(\frac{\pi\theta}{\alpha}\right) \hat{\boldsymbol{\theta}} \right] \quad (32)$$

respectively. Therefore, similar to the  $\phi$  field, the  $\psi$  field also has an integrable singularity at the corner when  $\alpha > \pi$ .

The effect of this singular behavior is local and does not affect the convergence of our numerical scheme, which solves for the values of  $\psi$  and  $\phi$  in the given domain. However, the numerical solution will not be very accurate in the vicinity of the corners with  $\alpha > \pi$ . When the flow is driven by the electric potential  $\phi$ , the velocities will be very large near the corner of  $\alpha > \pi$  due to the singularity of  $\nabla\phi$  at the corner. Earlier we had assumed that the redistribution of charged species due to the convection will be negligible if the flow velocity is not too large. This assumption may not be valid in the vicinity of the corner.

It was mentioned before that the redistribution of charged species due to the convection is negligible if the Debye thickness is small compared to the "external" length scale of the problem (e.g., the length scale of the variation of  $\phi$ ). We will elaborate on this assumption now. Consider a wall with a constant value of zeta potential  $\psi_w$ . The solution for the surface charge potential,  $\psi$ , will be such that the lines of constant  $\psi$  will run parallel along the walls where  $\psi = \psi_w$ . Besides, for small Debye thickness, the  $\psi$  field decays exponentially away from the wall. From (14) we note that the lines of constant charge are the same as the lines of constant  $\psi$  and thus run parallel along the walls. For the external potential field,  $\phi$ , the insulation boundary condition was imposed at the walls. Thus, the constant  $\phi$  lines will be perpendicular to the wall, or the direction of the gradient  $\nabla\phi$  will be along the wall. From (16) we know that the fluid is subjected to a body force in the direction of  $\nabla\phi$ . One only need to consider the body force on the fluid within the Debye layer, since outside the Debye length the charge density is negligible giving rise to negligible body force. Therefore, for a small Debye thickness, the body force will act along the constant charge lines within the entire Debye layer; thus the streamlines will be parallel to these constant charge lines. This causes the charged species to convect along the constant charge lines giving rise to negligible charge redistribution.

For the flow around a corner with  $\alpha > \pi$ , the Debye thickness may not be small compared to the external length scale. It may be inappropriate to assume the Debye thickness to be small near the corners with  $\alpha > \pi$ . Charge redistribution may become important in the vicinity of the corner.

Although the arguments presented above are by no means rigorous, they provide considerable physical insight into the validity of the assumptions made earlier. Despite the shortcomings mentioned above, the qualitative nature of the electroosmotic flow field away from the corners will not be greatly affected.

## NUMERICAL SCHEME

The equations in (16) were solved using the semiimplicit method for pressure-linked equations revised (SIMPLER) algorithm developed by Patankar.<sup>18</sup> This algorithm has been successfully implemented for many problems of Newtonian fluid flow and heat transfer in both laminar and turbulent situations. The

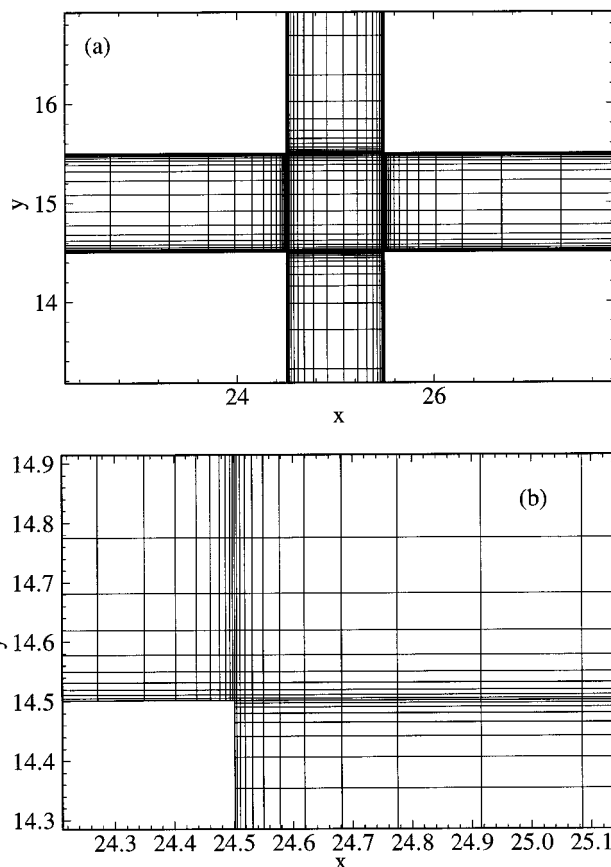


Figure 4. Nonuniform grid generated in the cross-channel geometry: (a) far-off view; (b) close-up of the grid at one of the corners.

algorithm is based on a finite volume discretization of the governing equations on a staggered grid.

In our implementation, the solution to the nonlinearly coupled equations is obtained through an iterative procedure. During each iteration, the discretized equations are first solved by a block correction procedure in the three ( $x, y, z$ ) directions. Then six sweeps of line-by-line iterations are performed, in which the equations are written as a scalar tridiagonal system along each grid line and solved directly using the tridiagonal matrix algorithm (TDMA).

A two-dimensional flow solver for SIMPLER is well distributed among the academic community. Since we intended to test a three-dimensional code, we developed the flow solver capable of handling three-dimensional problems in rectilinear and cylindrical coordinate systems. The code was tested by solving problems given in ref 18 (see chapter 9) and comparing the results with those given in the literature (references available in ref 18).

We generate a structured grid within the computational domain. In the problem at hand, there are primarily three length scales. They are the length scale of the Debye thickness, the length scale of the channel width, and the length scale of the distance between the reservoirs 1 and 2 across which the external potential is applied. Since the Debye thickness is very small compared to the channel width, a very fine grid is required near the walls to capture the variation of the velocity profile in that region. We generate a nonuniform grid such that the control volume size is minimum next to the walls (Figure 4a). The size of successive control volumes away from the walls is increased

(18) Patankar, S. V. *Numerical Heat Transfer and Fluid Flow*; Hemisphere Publishing Corp.: New York, 1980.

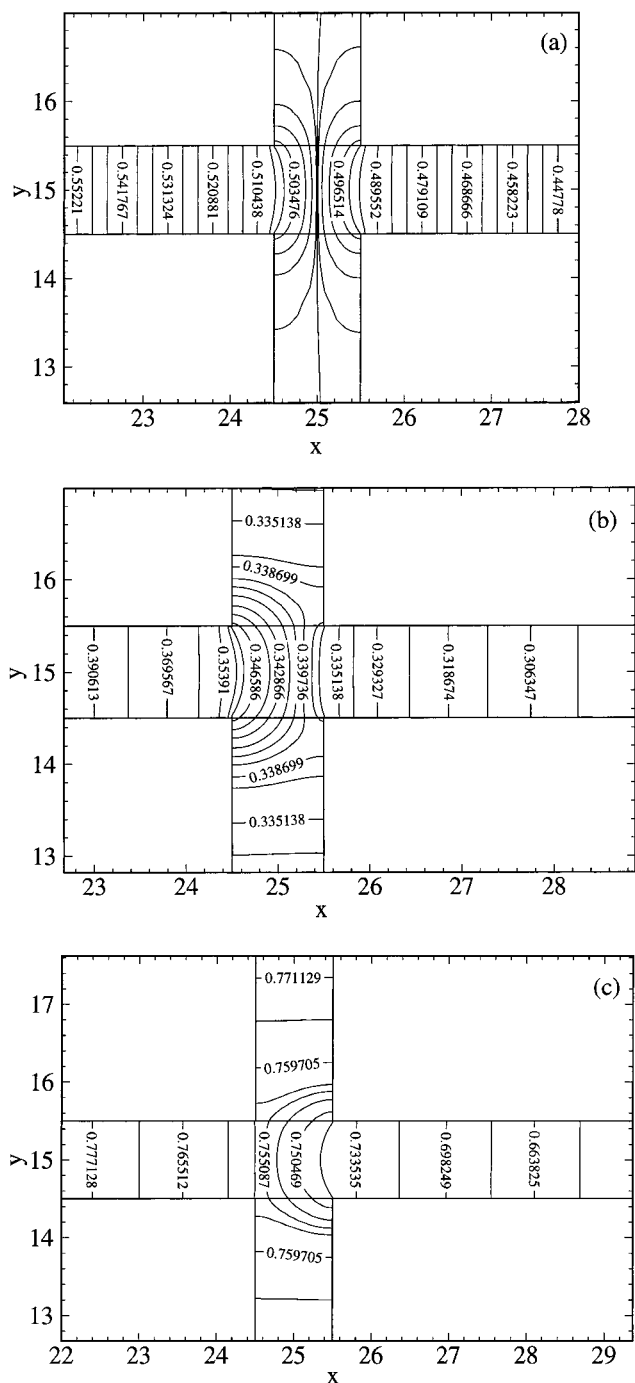


Figure 5. External potential field inside the cross-channel. Potential at the side reservoirs: (a) 0.5, (b) 0.25, and (c) 0.9.

by a factor of 1.5. A closer view of the mesh near the wall is shown in Figure 4b. Similar refinement is done in the vicinity of the top and bottom walls. All the results are presented by using the nondimensional variables.

The Debye thickness ( $\kappa^{-1}$ ) is usually of the order  $10^{-9}$  m; hence, for the geometry being studied (the device used by Fan and Harrison<sup>4</sup>), the nondimensional Debye thickness is  $(\kappa h)^{-1} = 3.3 \times 10^{-5}$ . It is computationally very costly to capture the velocity profile at such a fine length scales. Since we are only interested in the qualitative nature of the flow pattern, we restrict the nondimensional Debye thickness to be  $\sim 5 \times 10^{-2}$ . With these parameters, 50Mbytes of RAM was required to run the program.

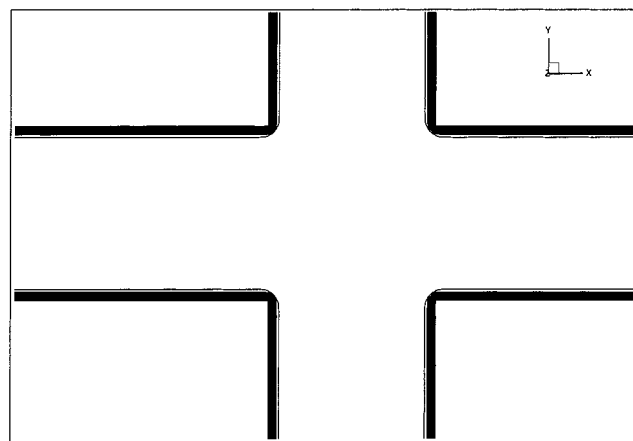


Figure 6. Contour plot of  $\psi$  at  $z = 1/6$  (midplane in the  $z$ -direction),  $z = 0$  is the bottom wall.

It took  $\sim 180$  min on a SGI R4000 machine to complete one steady-state calculation.

## NUMERICAL RESULTS

In this section we will present our numerical results. We have studied the effect of the Reynolds number, the electric potential, and the pressure at the side reservoirs on the flow field.

**External Potential Field.** Figure 5 shows the external potential field inside the cross-channel at different values of the applied potential at the side reservoirs 3 and 4. Reservoir 1 is always at potential 1 and reservoir 2 is at 0 potential. When the potential at the side reservoirs is 0.5, we see that by symmetry the potential at the center of the cross-channels is also 0.5. As a result, there are only small variations of potential in the side channels. Hence the body force acting on the fluid in the side channels is very small. As a result there is no flow to or from the side reservoirs in this situation.

When the potential at the side reservoirs is varied, we see that the potential at the center of the intersection is no longer 0.5. It is greater than (or less than) 0.5 if the potential at the side reservoir is greater than (or less than) 0.5 (Figure 5b,c). There is also a potential gradient in the side channels indicating that there will be a flow to or from the side reservoirs. This gradient becomes stronger as the potential at the side reservoirs is varied further away from the value of 0.5.

There is no variation of  $\phi$  in the  $z$ -direction due to the insulation boundary conditions on the top and bottom walls.

**Potential due to the Charge on the Walls.** Figure 6 shows the numerical solution of the potential due to charge on the walls. As expected, we notice that the contour lines are densely packed (dark region in the plot) only next to the wall indicating a sharp decay in potential away from the walls. This solution is the same for all cases we have simulated since the value of the  $\zeta$  potential and the Debye thickness are kept constant.

Similar decay of  $\psi$  field is observed near the top and bottom walls. The nature of the decay of  $\psi$  field is exponential and changes from a value (nondimensional) of one at the walls to a value of zero away from the walls.

**Flow Field at Varying Reynolds Numbers.** To understand the effects of the Reynolds number, we computed the flow field with the potential at the side reservoirs set to 0.5 and the pressure at all the reservoirs set to 0. Figure 7 shows a velocity vector plot inside the injection channel. The nondimensional magnitude of the maximum velocity in the channel is of order 1. We see that the velocity changes very sharply near the walls and stays

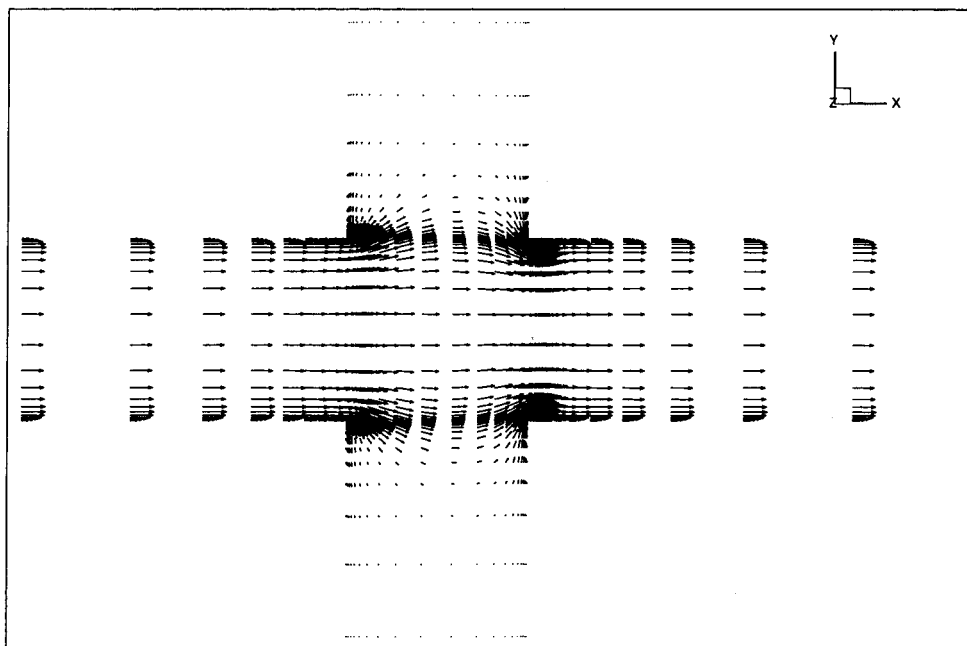


Figure 7. Velocity vector plot at the channel intersection:  $Re = 100$ ,  $\phi = 0.5$ , and  $p = 0$  at the side reservoirs.

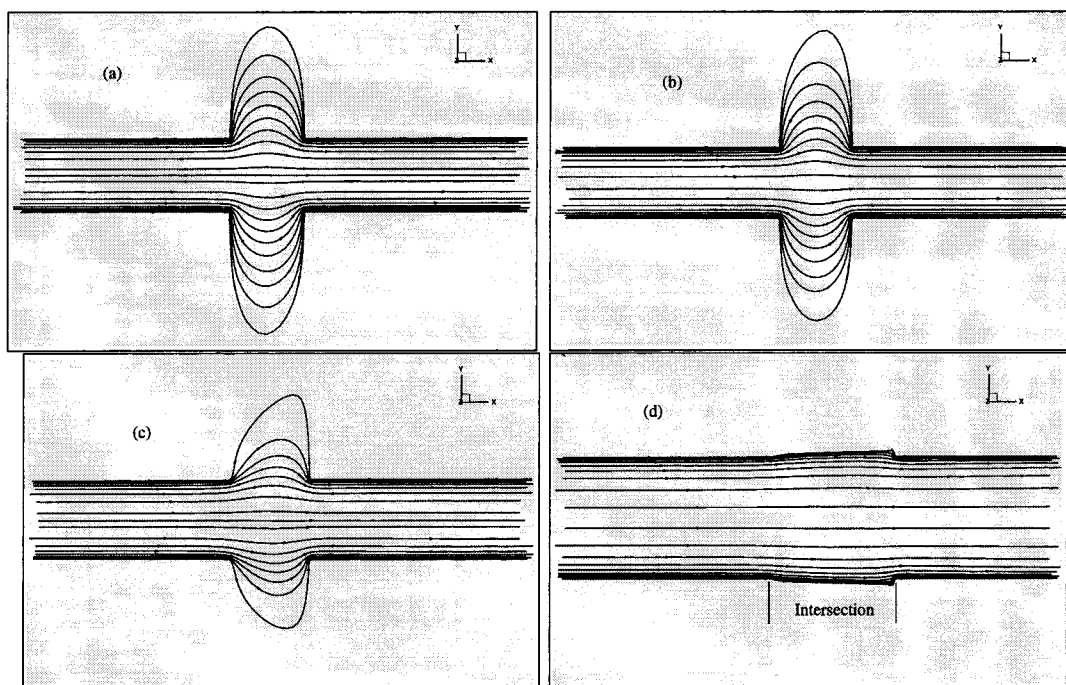


Figure 8. Effect of Reynolds number on the streamlines at the intersection of the channels:  $\phi = 0.5$  and  $p = 0$  at the side reservoirs.  $Re =$  (a) 0.1, (b) 10, (c) 100, and (d) 1000.

constant in the rest of the channel. The variation in the velocity profile around the intersection of the channels is due to the local pressure variation.

It is difficult to visualize the three-dimensional streamlines (which are the same as the particle path lines in the steady state). However, our three-dimensional simulations have shown that the velocity component in the  $z$ -direction is very small. Consequently, the fluid moves in layers on the  $x$ - $y$  plane (or constant  $z$ -planes). The streamlines in any  $z$ -plane would give a good picture for the flow field. Hence we will present the results by plotting the streamlines of the flow only at the midplane in the  $z$ -direction. Figure 8 shows the streamlines at various Reynolds numbers.

Please note that the relative spacing between the streamlines (or the path lines) is in no way related to the magnitude of the velocity at that location. We have greater density of streamlines near the walls because the grid is finer in that region. It is seen that the streamlines "straighten up" as the Reynolds number is increased. In fact, at  $Re = 1000$  there is hardly any distortion of the streamlines. Thus the injection at high Reynolds numbers should give a better shape of the sample plug at the intersection of the channels. The size of the sample plug also depends on the Reynolds number. When the Reynolds number is low, the sample is more distorted and at the same time it is bigger in size. The value of the Reynolds number depends on the intensity of the

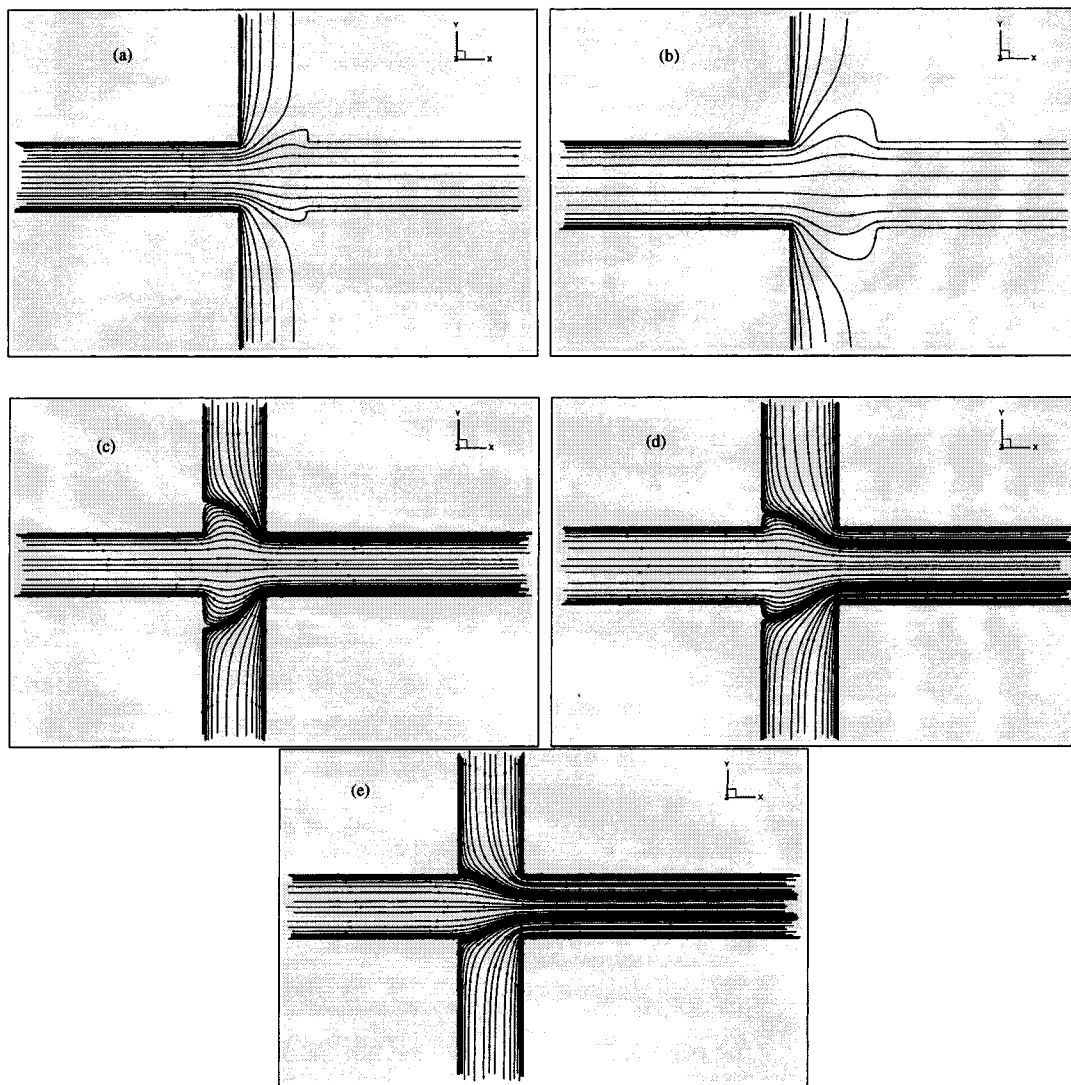


Figure 9. Effect of different values of  $\phi$  at the side reservoirs on the streamlines at the intersection.  $p = 0$  at the side reservoirs and  $Re = 0.1$ .  $\phi =$  (a) 0.25, (b) 0.4, (c) 0.60, (d) 0.75, and (e) 0.90 at reservoirs 3 and 4.

applied electric field. Thus, we see that as the intensity of the electric field is increased the volume of the injected sample at the intersection decreases. Fan and Harrison<sup>4</sup> observed some variation in the injection volume as a function of the applied electric field. They further remarked that such an observation was unexpected since the volume injected should have been defined only by the intersection volume and diffusion into the side channels. This is true when the Reynolds number is low. Our simulations show that at higher values of Reynolds number the injection volume decreases with the applied electric field.

Very high Reynolds number injection may not be possible in experiments. We estimate the value of the Reynolds number in the previous experimental works. We assume that the buffer solution has the similar physical properties as water,

$$\left. \begin{aligned} \epsilon &\sim 6.95 \times 10^{-10} \text{ C}^2/\text{J}\cdot\text{m} \\ \zeta &\sim 100 \text{ mV} \\ \mu &\sim 10^{-3} \text{ N}\cdot\text{s}/\text{m}^2 \\ \rho &\sim 10^3 \text{ kg}/\text{m}^3 \\ \varphi/H &\sim 10^5 \text{ V}/\text{m} \\ h &= 30\text{--}70 \text{ }\mu\text{m} \end{aligned} \right\} \quad (33)$$

These values give rise to a Reynolds number of order 1. The value of the Reynolds number can be increased by applying a higher voltage across the device. This may not be possible since the device may not be able to sustain such a high voltage. Hence, alternative methods to control the shape of the sample plug are necessary. Applications of the electric potential or the pressure at the side reservoirs are two possibilities.

We also note that at higher Reynolds numbers the charge redistribution can become important when the Debye thickness is not very small. Such cases may generate different flow characteristics.

**Effect of External Potential at the Side Reservoirs.** To study this case, we fix the Reynolds number at  $Re = 0.1$ , which is close to the experimental value. The values of the pressure at all the reservoirs are set to 0. We know that there is no flow to or from the side reservoirs when the potential at the side reservoirs is set to 0.5 (see Figure 8a).

We first set the potential at the side reservoirs to values less than 0.5. Panels a and b of Figure 9 show that there is a flow of fluid from the injection channel into the side channels. This can be easily explained by noting that there is a gradient of potential in the side channels (Figure 5b) which drives the fluid into the side reservoirs. Such a flow is undesirable during the injection,

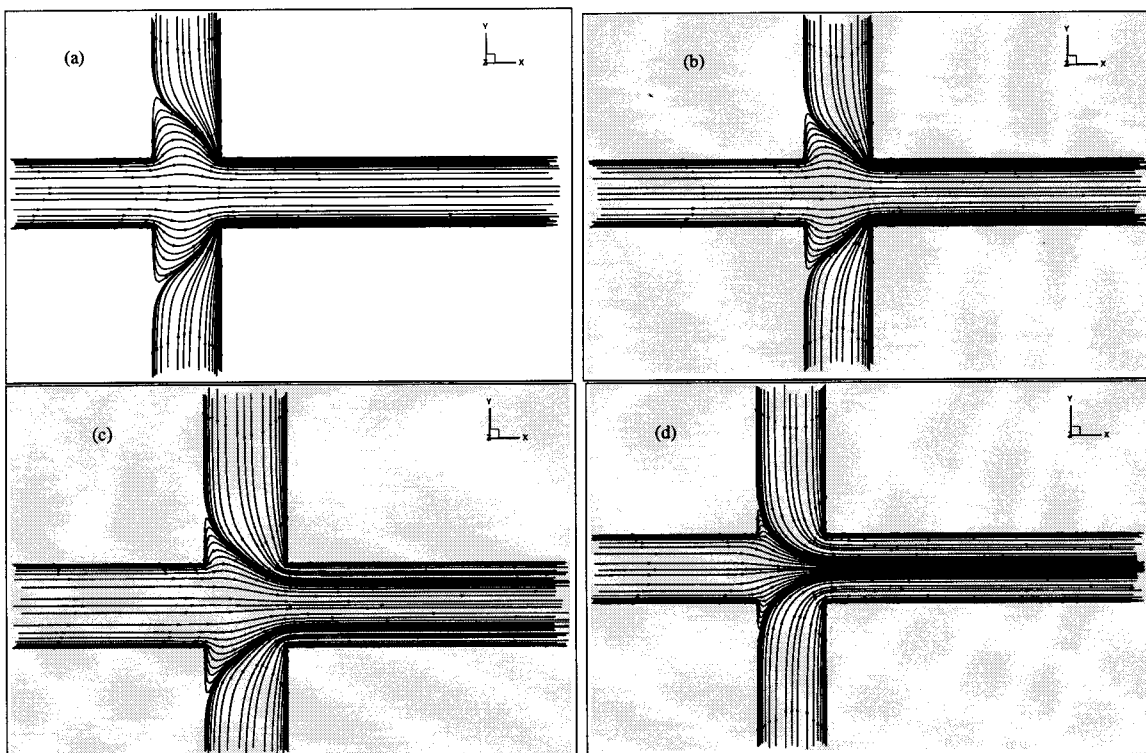


Figure 10. Effect of different values of pressure at the side reservoirs on the streamlines at the intersection.  $\phi = 0.5$  at the side reservoirs and  $Re = 0.1$ .  $p =$  (a) 250, (b) 500, (c) 1000, and (d) 2000 at reservoirs 3 and 4.

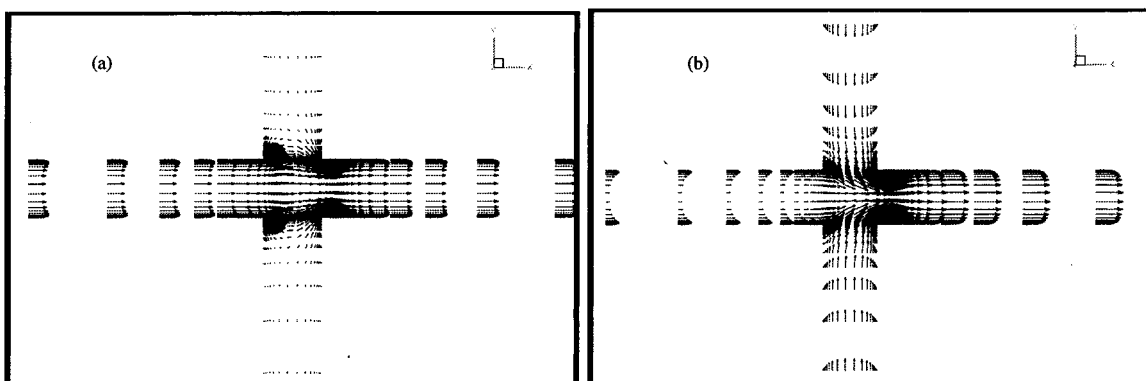


Figure 11. Effect of different values of pressure at the side reservoirs on the velocity profile in the channel.  $\phi = 0.5$  at the side reservoirs and  $Re = 0.1$ .  $p =$  (a) 250 and (b) 2000 at reservoirs 3 and 4.

since instead of a sample plug at the channel intersection the sample solution will run into the side channels (which is used as the separation channel later) and “contaminate” the buffer solution.

We next set the potential at the side reservoirs to values greater than 0.5. Panels c–e of Figure 9 show that the fluid flows from the side channels into the injection channel due to the gradient of  $\phi$  in the side channels. The streamlines in the injection channel are squeezed at the intersection by the fluid coming in from the side channels. This is desirable since the sample will now be restricted to remain near the intersection of the channels. However, if the potential at the side reservoirs is too high, the streamlines from the injection channel will be squeezed too much (Figure 9e), generating a larger distortion to the sample plug at the intersection. We observe, from Figure 9, that a potential equal to 0.75 at the side reservoirs give the best result.

This technique of controlling the shape of the sample at the intersection by applying potential at the side reservoirs has been used in experiments. Our simulations further elaborate the flow field under such conditions and help in identifying the most suitable value of the potential for a given setup.

**Effect of Pressure at the Side Reservoirs.** Another way of controlling the shape of the sample at the intersection is by applying the pressure at the side reservoirs. In simulating this case, we set the Reynolds number  $Re = 0.1$  and the potential at the side reservoirs to 0.5.

A positive pressure at reservoirs 3 and 4 drives the flow toward the intersection of the channels since reservoirs 1 and 2 are at 0 pressure. This is depicted in Figure 10. The flow from the side channels squeezes the streamlines in the injection channel. This gives a better sample plug at the intersection. Very high pressures at the side reservoirs are not desirable since the streamlines from

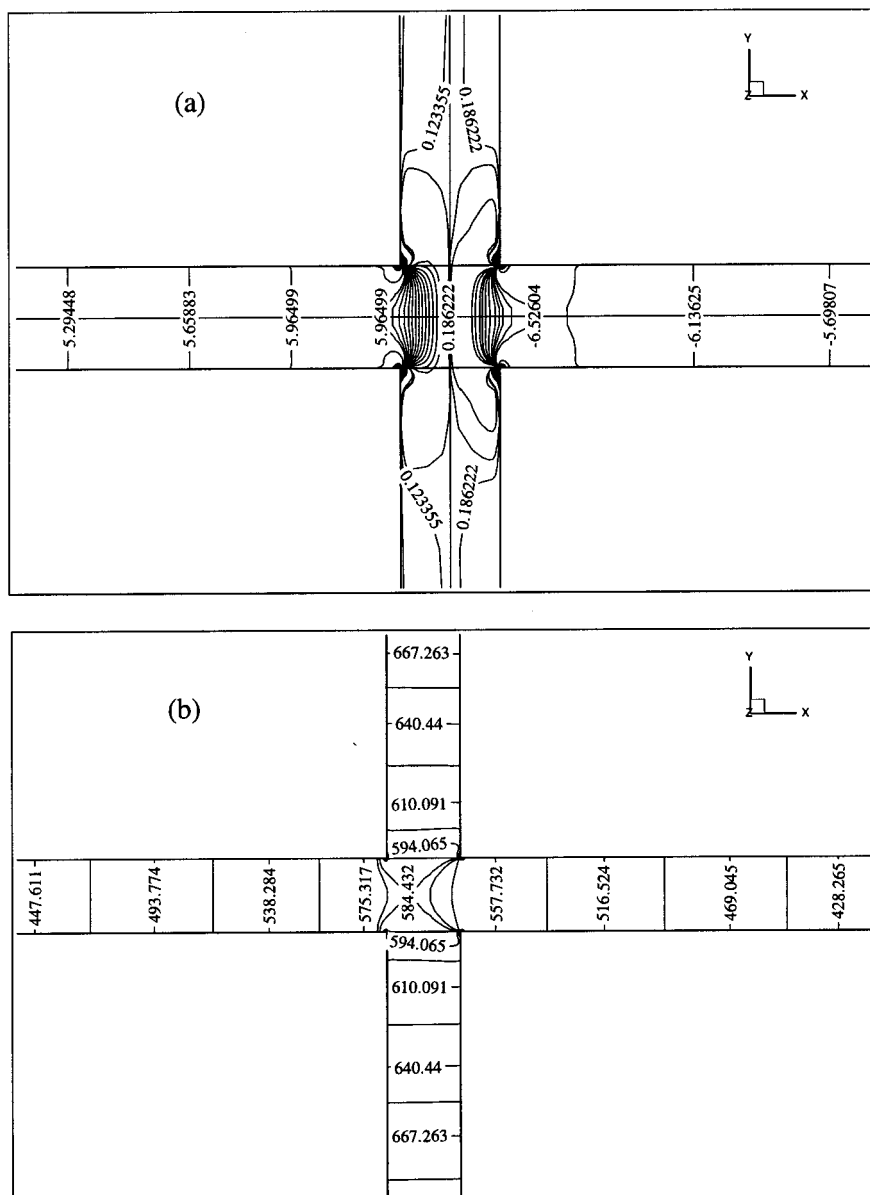


Figure 12. Contour plot of pressure inside the channel at different values of pressure at the side reservoirs.  $\phi = 0.5$  at the side reservoirs and  $Re = 0.1$ .  $p =$  (a) 0 and (b) 1000 at reservoirs 3 and 4.

the main channel can be squeezed too much (Figure 10d).

Comparison between the shape of the squeezed streamlines in Figures 9 and 10 shows that applying pressure at the side reservoirs causes a greater distortion of the streamlines at the intersection. Thus it may be more desirable to control the shape of the sample at the intersection by applying the potential at the side reservoirs rather than by applying the pressure.

Figure 11 shows the velocity profile in the channels for different values of pressure at the side reservoirs. We observe that the application of high pressures at the side reservoirs causes a considerable back pressure on the flow in the injection channel between the intersection and the reservoir 1. This distorts the velocity profile in the injection channel such that the velocity in the middle of the channel is decreased. This may not be a desirable feature during the injection since it will take longer for the injection process.

Figure 12 plots the pressure field in the cross-channel for different values of the pressure at the side reservoirs. When the

pressure at the side reservoirs is 0, there is negligible variation of pressure within the side channels (Figure 12a). Thus we see no net flow to or from the side reservoirs (Figure 8a). Application of a positive pressure at the side reservoirs gives rise to a pressure gradient within the side channels (Figure 12b). This causes an inflow from the side reservoirs (Figure 10c).

Next, we consider a case when there is no external pressure gradient applied on the device. For this case, the boundary condition given in (20) is true if the reservoirs are infinitely large. This is because any flow into or out of the reservoir keeps it at a "stationary" state so that the pressure at channel entrance is not changed. This condition may not be exactly satisfied in experiments. As a result, flows are induced in these reservoirs. This gives rise to variations of the pressure inside the reservoirs. Such pressure difference may become important in the side channels when there is no electroosmotic flow (i.e., when the potential at the side reservoirs is 0.5 in our case). These "induced" pressure gradients may generate a flow into the injection channel from the

side channels. This has been observed in experiments by Fan and Harrison<sup>4</sup> and was referred to as the leakage flow. This leakage flow will be qualitatively similar to the flow shown in Figure 10. The amount of leakage will depend on the device and can possibly be characterized.

#### CONCLUSIONS

1. We have developed a three-dimensional numerical scheme to simulate electroosmotic flows. Using this scheme, we have studied the injection of the sample solution in a cross-channel device for capillary electrophoresis.

2. Our simulations show that the distortion of the injected sample at the intersection of the cross-channel is reduced when the injection is performed at higher Reynolds numbers (at higher electric field intensities).

3. Our simulations also show that the application of an electric potential at the side reservoirs can be used to control the shape of the injected sample plug. This potential at the side reservoirs should be greater than the potential at the center of intersection so that there is a flow of the buffer solution into the injection channel from the side reservoirs.

4. The shape of the sample plug can also be controlled by applying a pressure at the side reservoirs. However, the distortion of the sample plug obtained by applying the pressure is greater as compared to that obtained by applying potential at the side reservoirs.

As a part of future work, we suggest unsteady simulations since the duration of the injection is seen to affect the separation efficiency in experiments. Our steady-state simulations did not provide insight into this.

#### ACKNOWLEDGMENT

This work was supported by the National Science Foundation under Grant ECS-9527123 and CTS 94-10022 and by the Research Foundation of the University of Pennsylvania.

Received for review August 5, 1997. Accepted February 16, 1998.

AC970846U